

NOVEL SOLAR SAIL MISSION CONCEPTS FOR SPACE WEATHER FORECASTING

Jeannette Heiligers,^{*} and Colin R. McInnes[†]

This paper proposes two novel solar sail concepts for space weather forecasting: heliocentric Earth-following orbits and Sun-Earth line confined solar sail manifolds. The first concept exploits a solar sail acceleration to rotate the argument of perihelion such that aphelion, where extended observations can take place, is always located along the Sun-Earth line. The second concept exploits a solar sail acceleration to keep the unstable, sunward manifolds of a solar sail Halo orbit around a sub- L_1 point close to the Sun-Earth line. By travelling upstream of space weather events, these manifolds then allow early warnings for such events. The orbital dynamics involved with both concepts will be investigated and the observation conditions in terms of the time spent within a predefined surveillance zone are evaluated. All analyses are carried out for current sail technology (i.e. Sunjammer sail performance) to make the proposed concepts feasible in the near-term. The heliocentric Earth-following orbits show a reasonable increase in useful observation time over inertially fixed, Keplerian orbits, while the manifold concept enables a significant increase in the warning time for space weather events compared to existing satellites at the classical L_1 point.

INTRODUCTION

Solar coronal mass ejections are believed to be the cause of magnetic storms that can have detrimental effects on vital assets on ground and in space: destruction of power grids leading to power outages, damage to oil pipelines, need for aviation re-routing, damage to Earth-orbiting satellites and hazardous conditions for astronauts onboard the International Space Station. Measurements taken by spacecraft located in a Halo orbit around the classical L_1 point (SOHO (ESA/NASA, 1996), ACE (NASA, 1997) and WIND (NASA, 2004)), are used to warn operators for these events. However, warning times from these satellites are only 30-60 minutes, which leaves little time to take appropriate action.

As alternative to the L_1 point, many other concepts can be found in the literature that aim at space weather monitoring and/or forecasting. These concepts are Earth orbiting, Sun orbiting or orbiting an artificial Lagrange point. Examples of the Earth orbiting type include the use of nanosats [1], cubsats [2] and microsats [3] in low-Earth orbital constellations to monitor key space weather parameters in the Earth's vicinity. The Solar Polar [4, 5] and Helix missions [6] were proposed to orbit the Sun and would be used to

^{*} Research Associate, Advanced Space Concepts Laboratory, Department of Mechanical and Aerospace Engineering, University of Strathclyde, 75 Montrose Street, Glasgow, G1 1XJ, U.K., jeannette.heiligers@strath.ac.uk.

[†] Director, Advanced Space Concepts Laboratory, Department of Mechanical and Aerospace Engineering, University of Strathclyde, 75 Montrose Street, Glasgow, G1 1XJ, U.K., colin.mcinnnes@strath.ac.uk.

understand the structures and features of the Sun, the initiation, evolution and propagation of coronal mass ejections and the tracking of eruptions all the way from the surface of the Sun to the Earth.

Studies similar to the upcoming Sunjammer mission* that targets a sub- L_1 point sunward of the classical L_1 point, are the Geostorm mission [7] as well as more general sub- L_1 investigations. [8, 9] A more extensive application of the Geostorm concept was proposed by Sauer [10] where four solar sail spacecraft are placed in a diamond arrangement at the sub- L_1 point. This would allow multipoint measurements to determine the large scale three-dimensional structure of solar disturbances propagating toward the Earth.

The Sunjammer mission, as well as the Geostorm concept and the concept proposed by Sauer make use of solar sails. Although the idea of solar sailing has been around since it was suggested by Tsiolkovsky in 1921, only recently, in 2010, was solar sail propulsion demonstrated in space by JAXA's IKAROS mission. [11] Due to its success, as well as that of NASA's NanoSail-D2 mission [12], research in the field of solar sailing is flourishing. It is driven by the huge potential of solar sail missions as they are not constrained by propellant mass: solar sailing exploits the radiation pressure generated by solar photons reflecting off a large, highly reflecting sail to produce a continuous thrust acceleration. With the Sun as 'propellant' source, solar sail missions have in principle infinite lifetime. [13] With more solar sail missions scheduled within the next few years, including NASA's Sunjammer mission* and The Planetary Society's LightSail mission [14], solar sail technology truly is gaining momentum.

In this paper, the use of solar sailing will be further exploited to complement the space weather monitoring and forecasting concepts found in the literature. In particular, two concepts will be explored: heliocentric Earth-following orbits and Sun-Earth line confined solar sail manifolds.

The heliocentric Earth-following orbits rely on a solar sail acceleration to rotate the argument of perihelion of an eccentric planar orbit such that aphelion is always located along the Sun-Earth line. Since the orbital velocity at aphelion is relatively small, these orbits allow extended observations of space weather events traveling toward the Earth. Compared to Keplerian elliptic orbits that are inertially fixed and therefore have aphelion aligned with the Sun-Earth line only once per synodic period of the Earth-sail system, this concept creates an increase in the coverage of the Sun-Earth line.

The second concept, Sun-Earth line confined solar sail manifolds, exploit the unstable sunward manifolds of a solar sail Halo orbit around an artificial Lagrange point, or sub- L_1 point, to travel upstream of the coronal mass ejections and increase the warning time for space weather events over measurements from the (sub)- L_1 point. Since the manifolds eventually move away from the Sun-Earth line, the idea is to provide a constant disposal of small SpaceChips [15] from a carrier spacecraft to replenish the manifolds. These SpaceChips have a large area-to-mass ratio, similar to a solar sail, and can therefore exploit solar radiation pressure in a similar manner. [16] Alternatively, small nanosats with deployable solar sails could be used for the same purpose or a conventional sailcraft like Sunjammer could be inserted into one of the manifolds towards the end-of-life to allow improved observations at the end of the mission. The concept of using manifolds in this particular way was first proposed by K echichian and co-authors [17], but was only considered for the classical case, i.e. for ballistic manifolds winding off a Halo orbit around the classical L_1 point. This paper will therefore show the improvements that can be achieved by adding a solar sail acceleration to the concept.

The paper is divided into two main sections, each one devoted to one of the two novel concepts. First, the heliocentric Earth-following orbits will be investigated: the orbital configuration and constraints are derived. A simple apsides steering law is first assumed. By furthermore assuming that the semi-major axis and eccentricity do not change during one orbital revolution, analytic results on the achievable heliocentric Earth-following orbits for particular solar sail performances can be derived. By removing this assumption, a numerical analysis provides more realistic results and shows that a Sunjammer-type sail can increase the time spent within a predefined surveillance zone around the Sun-Earth line by a factor 1.18 compared to an

* Sunjammer mission, <http://www.sunjammermission.com/>, Retrieved 14 January 2014.

equally sized, inertially fixed Keplerian orbit. This factor is increased further to 1.29 by finding the optimal steering law in the heliocentric Earth-following orbit.

Secondly, the Sun-Earth line confined solar sail manifolds are investigated: the circular restricted three-body problem is defined, artificial equilibrium points are introduced, the sub- L_1 points for the Sunjammer sail performance are derived and solar sail Halo orbits around these sub- L_1 points are obtained. Orbits, equal in size to the orbit considered by K echichian and co-authors, are selected for a fair comparison and the unstable sunward manifolds of these Halo orbits are investigated. Three different steering laws are assumed in the manifolds: 1) a sail attitude perpendicular to the Sun; 2) a constant sail attitude pitched with respect to the Sun-Earth line; and 3) the optimal solar sail steering law to reach as far as possible upstream of the coronal mass ejections. As will be shown, the second and third steering laws enable significant improvements over observations currently being taken from L_1 and also compared to the ballistic results found by K echichian and co-authors: maximum warning times of 4.5-9 hours can be obtained with a solar sail, which is a major step forward from the 30-60 minutes currently feasible from satellites at L_1 .

HELIOCENTRIC EARTH-FOLLOWING ORBITS

The concept of heliocentric Earth-following orbits is illustrated in Figure 1: a solar sail acceleration a_s in direction \hat{n} is used to rotate the line of apsides of an elliptic heliocentric orbit such that aphelion follows the Sun-Earth line.

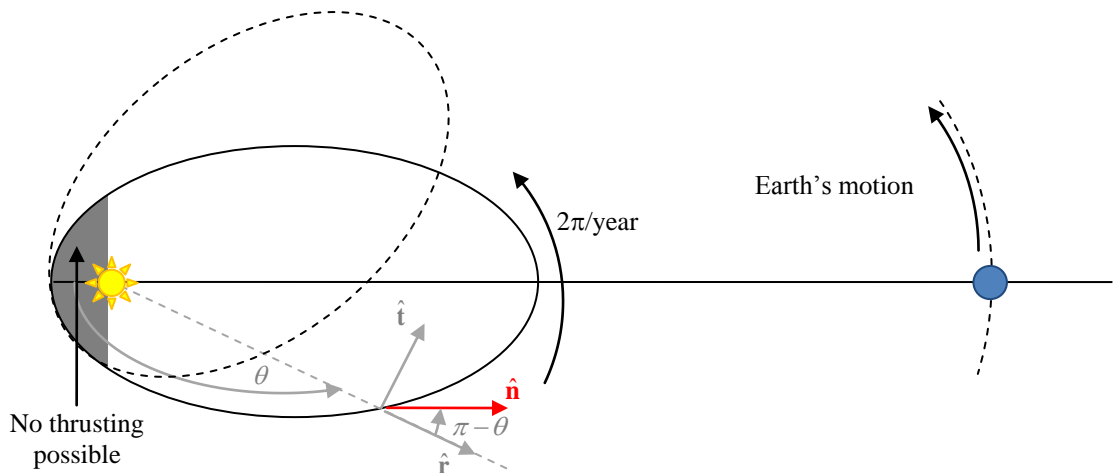


Figure 1 Illustration of heliocentric Earth-following orbits.

Since a planar case is considered (such that the solar sail orbits the Sun in the ecliptic plane), the evolution of the osculating orbital elements and time is given by the following four Lagrange equations: [18]

$$\begin{aligned}
 \frac{da}{d\theta} &= \frac{2pr^2}{\mu_s(1-e^2)^2} \left(e \sin \theta a_r + \frac{p}{r} a_t \right) \\
 \frac{de}{d\theta} &= \frac{r^2}{\mu_s} \left(\sin \theta a_r + \left(1 + \frac{r}{p} \right) \cos \theta a_t + e \frac{r}{p} a_t \right) \\
 \frac{d\omega}{d\theta} &= \frac{r^2}{\mu_s e} \left(-\cos \theta a_r + \left(1 + \frac{r}{p} \right) \sin \theta a_t \right) \\
 \frac{dt}{d\theta} &= \frac{r^2}{\sqrt{\mu_s p}} \left(1 - \frac{r^2}{\mu_s e} \left(\cos \theta a_r - \left(1 + \frac{r}{p} \right) \sin \theta a_t \right) \right)
 \end{aligned} \tag{1}$$

with $\mu_s = 1.3272 \times 10^{11} \text{ kg}^3/\text{s}^2$ the gravitational parameter of the Sun, $p = a(1 - e^2)$, $r = p/(1 + e \cos \theta)$ and a_r and a_t the radial and transverse components of the perturbing solar sail acceleration.

By definition, a heliocentric Earth-following orbit has to satisfy the following conditions:

$$\begin{aligned} a_0 &= a_f \\ e_0 &= e_f \\ \Delta\omega &= \Delta t \frac{2\pi}{1 \text{ yr}} = (t_f - t_0)n_E \end{aligned} \quad (2)$$

where the subscripts '0' and 'f' indicate the conditions at $\theta = 0$ and $\theta = 2\pi$ and n_E is the Earth's mean motion. The semi-major axis and eccentricity thus need to remain unchanged over one orbital revolution and the argument of perihelion needs to increase with the angular distance that the Earth traverses in time Δt . Here, Δt is the spacecraft orbital period (accounting for changes in the orbit period due to the perturbing solar sail acceleration). Note that the Earth's orbit is assumed to be circular.

The conditions in Eq. (2) can be satisfied by choosing a simple apsides steering law. An apsides steering law creates an acceleration opposite to the eccentricity vector, i.e. parallel to the (instantaneous) line of apsides and directed towards aphelion, see Figure 1. The radial and transverse components of the acceleration are then prescribed by:

$$\mathbf{a}_s = \begin{pmatrix} a_r \\ a_t \end{pmatrix} = a_s \begin{pmatrix} \cos(\pi - \theta) \\ \sin(\pi - \theta) \end{pmatrix} = a_s \begin{pmatrix} -\cos \theta \\ \sin \theta \end{pmatrix} \quad (3)$$

with

$$a_s = \beta \frac{\mu_s}{r^2} (\hat{\mathbf{r}} \cdot \hat{\mathbf{n}})^2 = \beta \frac{\mu_s}{r^2} \cos^2 \theta \quad (4)$$

Eq. (4) describes an ideal solar sail performance model, which assumes pure specular reflection of the impinging photons. The solar sail acceleration vector then acts perpendicular to the solar sail surface. The parameter β is the solar sail lightness number, which is the ratio of the solar radiation pressure acceleration and the solar gravitational acceleration. Or, equivalently, β can be expressed as a function of the sail area to spacecraft mass ratio, σ , and the critical solar sail loading parameter, $\sigma^* = 1.53 \text{ g/m}^2$:

$$\beta = \frac{\sigma}{\sigma^*} \quad (5)$$

The lightness number of the Sunjammer sail is known to be in the range 0.0388-0.0455 and will be used throughout this paper to assess the near-term performance of the proposed concepts. The extremes of this range will be indicated by $\beta_{SJ,low}$ and $\beta_{SJ,high}$, respectively.

A limitation of solar sails is their inability to generate an acceleration component in the direction of the Sun. [13] The steering law described in Eq. (3) can therefore not be maintained when $0 \leq \theta < \frac{1}{2}\pi$ or $\frac{3}{2}\pi < \theta \leq 2\pi$. Within these ranges, a different sail attitude is therefore assumed: turned edgewise to the Sun, and thus not producing an acceleration.

Substituting the adopted steering laws into Eq. (1) gives:

$$\left. \begin{aligned} \frac{da}{d\theta} &= \frac{2a}{1-e^2} \beta \cos^2 \theta \sin \theta \\ \frac{de}{d\theta} &= \beta \frac{\cos^3 \theta \sin \theta + e \cos^2 \theta \sin \theta}{1+e \cos \theta} \\ \frac{d\omega}{d\theta} &= \beta \frac{1}{e} \cos^2 \theta \left(1 + \frac{\sin^2 \theta}{1+e \cos \theta} \right) \\ \frac{dt}{d\theta} &= \frac{r^2}{\sqrt{\mu_s p}} \left(1 + \beta \frac{1}{e} \cos^2 \theta \left(1 + \frac{\sin^2 \theta}{1+e \cos \theta} \right) \right) \end{aligned} \right\} \frac{1}{2} \pi \leq \theta \leq \frac{3}{2} \pi \quad \left. \begin{aligned} \frac{da}{d\theta} &= 0 \\ \frac{de}{d\theta} &= 0 \\ \frac{d\omega}{d\theta} &= 0 \\ \frac{dt}{d\theta} &= \frac{r^2}{\sqrt{\mu_s p}} \end{aligned} \right\} \begin{aligned} 0 \leq \theta < \frac{1}{2} \pi \\ \frac{3}{2} \pi < \theta \leq 2\pi \end{aligned} \quad (6)$$

Time invariant semi-major axis and eccentricity

A first assessment of the heliocentric Earth-following orbits can be made by assuming that the semi-major axis and eccentricity do not change during the orbital motion. When keeping a and e constant, the equations for the argument of perihelion and time can be integrated analytically to obtain the change in these variables after one full revolution:

$$\Delta\omega = \frac{\beta}{6e^5} \left(-4e(-3+e^2) + 3\pi(2-e^2+e^4) - 12\pi(1+e) \sqrt{\frac{2}{1+e}} - 1 + 12\sqrt{1-e^2} \tan^{-1} \left(\frac{\sqrt{1-e^2}}{e} \right) \right) \quad (7)$$

$$\begin{aligned} \Delta t = \frac{a^2}{e^5 \sqrt{a\mu_s}} & \left(2e^5\pi + \beta \left((6e-3e^3-2\pi e^2+3\pi-\pi e^4) \sqrt{1-e^2} + (7e^2-6+2e^4)\pi \right) - \right. \\ & \left. - 2\beta(-6+7e^2+2e^4) \sin^{-1} \left(\sqrt{\frac{1-e}{2}} \right) \right) \end{aligned} \quad (8)$$

By substituting Eqs. (7) and (8) into the third equation of Eq. (2), the lightness number required to maintain a heliocentric Earth-following orbit can be obtained:

$$\beta = \frac{2a^2 e^5 n_E \pi}{a^2 n_E \left((-6+7e^2+2e^4) \left(2 \sin^{-1} \left(\sqrt{\frac{1-e}{2}} \right) - \pi \right) - (6e-3e^3-2\pi e^2+3\pi-e^4\pi) \sqrt{1-e^2} \right) - \frac{\sqrt{a\mu_s}}{6} \left(4e(-3+e^2) - 3\pi(2-e^2+e^4) + 12(1+e)\pi \sqrt{\frac{2}{1+e}} - 1 - 12\sqrt{1-e^2} \tan^{-1} \left(\frac{\sqrt{1-e^2}}{e} \right) \right)} \quad (9)$$

Since β is a function of the semi-major axis and eccentricity only, contours of equal lightness number can be drawn as shown in Figure 2a. The grey shaded area indicates a minimum required perihelion of 0.25 AU due to limitations on the thermal tolerance of the sail film. [13] Although the contours in Figure 2a extend up to large values for the lightness number, the validity of the results diminishes for such large sail accelerations since the Lagrange equations in Eq. (1) only hold when the perturbing acceleration is small compared to the gravitational acceleration.

Since the lightness number of the Sunjammer sail (and therefore the perturbing acceleration) is relatively small, Lagrange equations still hold for that performance range. The contours for $\beta_{SJ,low}$ and $\beta_{SJ,high}$ are shown in Figure 3a from which it is clear that a Sunjammer sail would only enable heliocentric Earth-

following orbits with small semi-major axes and small eccentricities. To maximize the relative time spent along the Sun-Earth line, the orbits with the maximum eccentricities (i.e. where the contours intersect the grey area) are considered for further investigations. Details of these orbits are given in Table 1. The evolution of this orbit for $\beta = \beta_{SJ,low}$, the steering law, argument of perihelion and dimensionless time are given in Figure 4. From Figure 4b (where the time is made dimensionless such that 1 year equals 2π), it is clear that the third condition in Eq. (2) is satisfied.

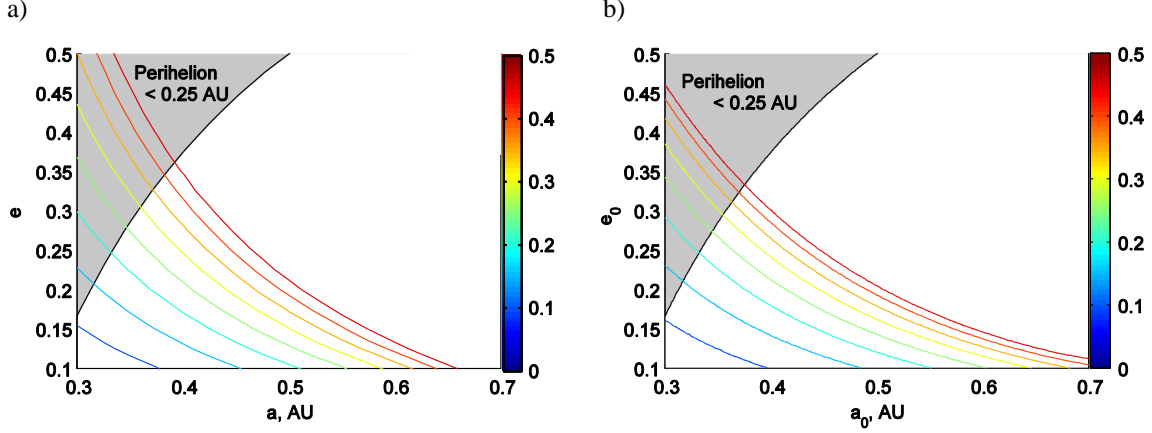


Figure 2 Contours of equal lightness number for $\beta = [0.1 \ 0.15 \ 0.2 \ 0.25 \ 0.3 \ 0.35 \ 0.4 \ 0.45]$ for heliocentric Earth-following orbits. a) Constant a and e . b) Time-varying a and e .

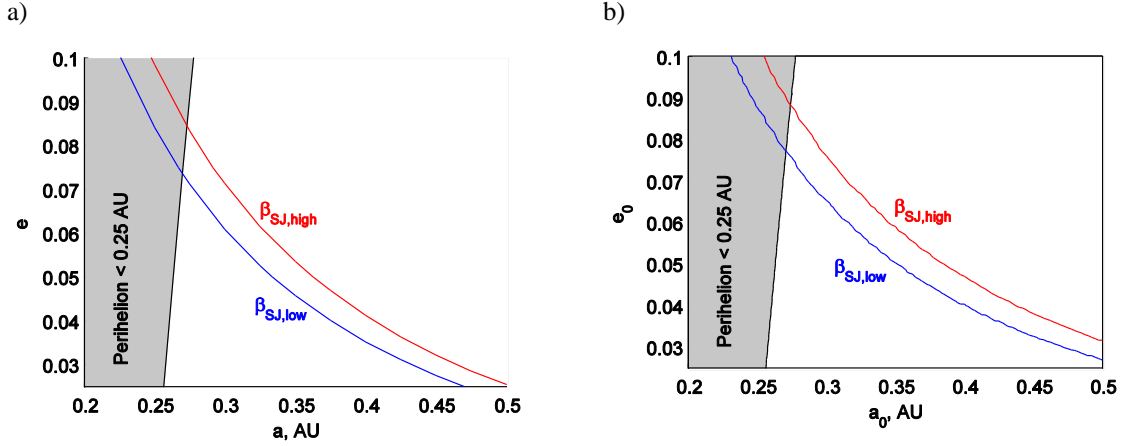


Figure 3 Contours of equal lightness number for $\beta = [0.0388 \ 0.0455]$ for heliocentric Earth-following orbits. a) Constant a and e . b) Time-varying a and e .

Table 1. Semi-major axis and eccentricity of selected heliocentric Earth-following orbits.

		Constant a and e	Time-varying a and e
$\beta = \beta_{SJ,low}$	a_0 , AU	0.2698	0.2708
	e_0	0.0736	0.0777
$\beta = \beta_{SJ,high}$	a_0	0.2728	0.2742
	e_0	0.0847	0.0888

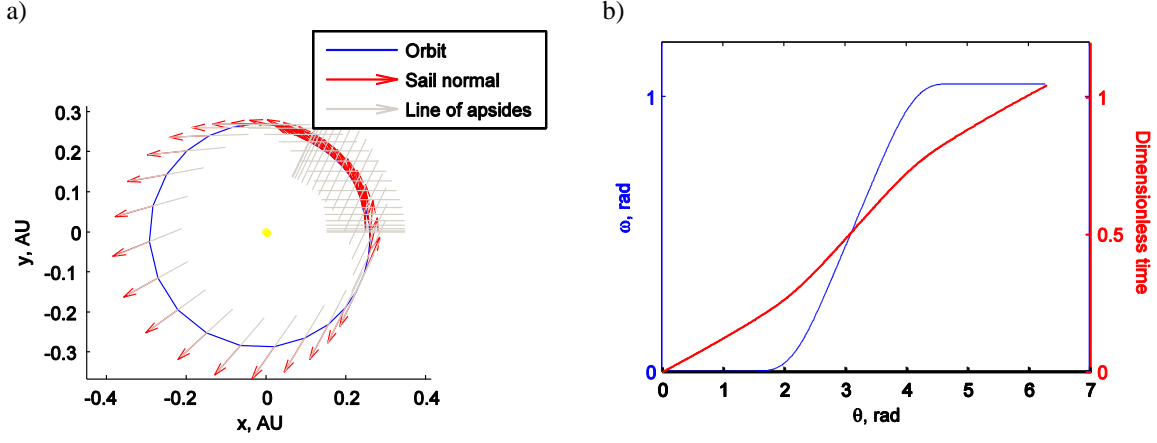


Figure 4 Heliocentric Earth-following orbits with constant $a = 0.2698$ AU and $e = 0.0736$ for $\beta = \beta_{SJ,low}$. a) Orbital evolution. b) Evolution of argument of perihelion and dimensionless time.

Time variant semi-major axis and eccentricity

The assumption of constant semi-major axis and eccentricity in the previous section allows an analytical investigation into the heliocentric Earth-following orbits. Removing this assumption and taking the actual variation in a and e into account, will have an effect on the performance of the solar sail. Since for time-varying a and e an analytic solution cannot be obtained from Eq. (6), a numerical approach is taken: a fine mesh in the initial value for a and e is considered (i.e. a_0 and e_0) and for each combination, the equations of motion are integrated for a range of β -values. For each value for β , the third condition in Eq. (2) is evaluated and the value that matches the condition closest is considered the required lightness number. The results are shown in Figure 2b, which clearly shows a difference with the results in Figure 2a that assumed constant a and e along the orbit. Interestingly, for small values of the lightness number, the performance seems to be improved. This is also clear from the contours for $\beta_{SJ,low}$ and $\beta_{SJ,high}$ in Figure 3b: the intersection between the contours and the grey area occurs at larger values for the semi-major axis and eccentricity. Details of the Keplerian elements of these orbits are also included in Table 1, while the evolution of the Keplerian elements during the orbit is provided in Figure 5 for $\beta = \beta_{SJ,low}$.

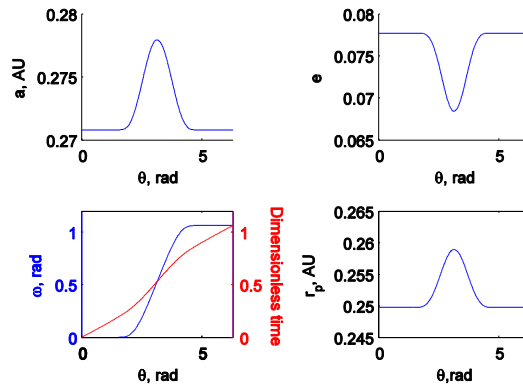


Figure 5 Evolution of Keplerian elements for heliocentric Earth-following orbits with time-varying a and e ($a_0 = 0.2708$ AU and $e_0 = 0.0777$) for $\beta = \beta_{SJ,low}$. r_p is the perihelion radius.

Surveillance zone analysis

In order to assess the performance of heliocentric Earth-following orbits for space weather applications, the amount of time spent by the spacecraft in a particular surveillance zone is considered. This surveillance zone is defined through the angle ε_{lim} which is measured from the Sun-Earth line (see Figure 6a). Whenever the spacecraft is located within this surveillance zone, it is assumed to be able to conduct useful space weather observations.

For comparison, the observation time achieved with an equally sized, Keplerian orbit is also considered. Since Keplerian orbits are inertially fixed, aphelion will only be aligned with the Sun-Earth line once per synodic period of the Earth-sail system. At other times, the Earth may be on the opposite side of the Earth when the spacecraft is at aphelion, losing out on valuable observation time.

For both the heliocentric Earth-following orbit as well as for the Keplerian reference orbit, the time spent within the surveillance zone depends on the initial orientation of the orbit with respect to the Sun-Earth line. This orientation is given by the initial value of the argument of perihelion, which is measured from the Sun-Earth line at time $t = 0$. For heliocentric Earth-following orbits the optimal orientation is $\omega_0 = \pi$. This is clear from the bottom left plot in Figure 5, which shows the symmetry in the orbit's evolution and the fact that aphelion is located at the instantaneous Sun-Earth line (i.e. the intersection of the two curves at $\theta = \pi$). For the Keplerian orbit it appears that the maximum observation time in the first orbital revolution is obtained when, again, aphelion coincides with the instantaneous Sun-Earth line, see Figure 6b. Since the orbit is inertially fixed, this means that ω_0 can be derived from the angular distance the Earth traverses in half the Keplerian orbital period, P_{orbit} . When using time in its dimensionless form, the argument of perihelion for the Keplerian reference orbit, ω_K , can thus be derived from:

$$\omega_K = \pi + \Delta t = \pi + \Delta t_{s/c} = \pi + \frac{1}{2} P_{\text{orbit}} \quad (10)$$

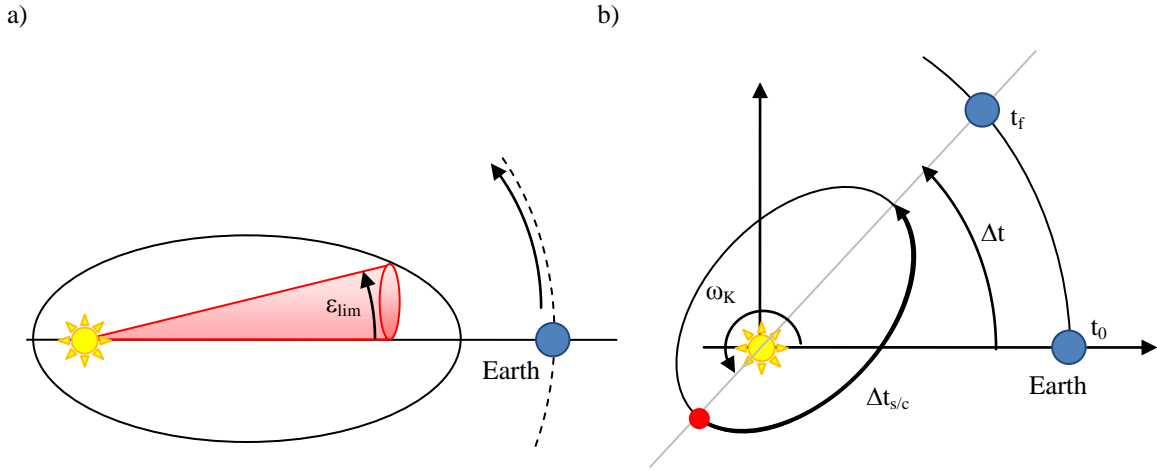


Figure 6 a) Definition of the space weather surveillance zone. b) Orbital geometry for Keplerian reference orbit.

The results of the surveillance zone analysis are provided in Figure 7 for both $\beta_{SJ,low}$ and $\beta_{SJ,high}$ and for three different values of ε_{lim} : 10, 20 and 45 degrees. From the observation time per orbit (plots a,b) it is immediately clear that, as expected, the heliocentric Earth-following orbits enable a constant number of days per orbit for useful observation since the Earth-sail configuration is the same for each orbital revolution. Also, as expected, the Keplerian reference orbit enables a good coverage during the first orbital revolution, but due to the fact that it is inertially fixed, much observation time is lost in subsequent orbits. This translates into a smaller overall percentage observation time for Keplerian orbits than for the heliocentric Earth-following orbits (plots c,d), e.g. for $\beta = \beta_{SJ,high}$ and $\varepsilon_{\text{lim}} = 45^\circ$, the overall percentages are 25.6 per-

cent and 30.1 percent, respectively. This means that the heliocentric Earth-following orbits allow 4.5 percent more observation time, or, equivalently, increase the observation time by a factor 1.18 compared to a Keplerian orbit. When inspecting the other results it appears that very similar factors hold for all cases, i.e. for $\beta = \beta_{SJ,low}$, $\beta = \beta_{SJ,high}$ and for each value for ϵ_{lim} .

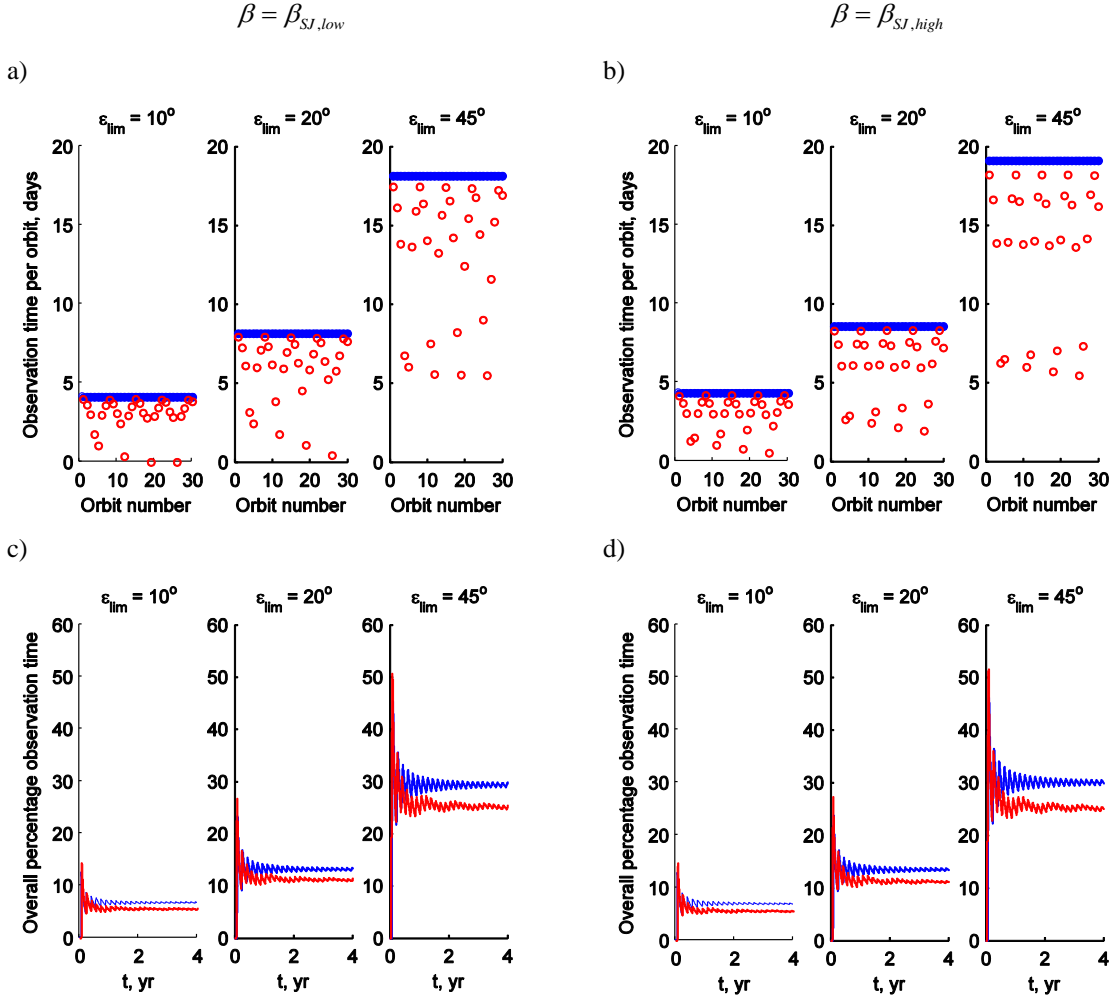


Figure 7 Surveillance zone analysis for $\beta = \beta_{SJ,low}$ (plots a,c) and $\beta = \beta_{SJ,high}$ (plots b,d). a-b) Observation time per orbit for heliocentric Earth-following orbits (blue solid markers) and Keplerian reference orbit (red open markers). c-d) Observation time as percentage of elapsed time for heliocentric Earth-following orbits (upper blue line) and Keplerian orbit (lower red line).

Optimal steering law

Although the apses steering law assumed in the previous section allows for a simple steering of the solar sail, it may not be optimal from an observation point of view. Therefore, to see whether the performance of heliocentric Earth-following orbits in this respect can be increased further, this section investigates what the optimal steering law should be to maximize the observation time. The optimal steering law is found by solving the accompanying optimal control problem using a particular implementation of a direct pseudospectral method in C++: PSOPT. [19] A condensed definition of the optimal control problem is given below.

The objective is to maximize the (initial) eccentricity of the heliocentric Earth-following orbit. This maximizes the difference between the orbital velocity at perihelion and aphelion. Then, the spacecraft spends relatively much time around aphelion, which eventually maximizes the percentage coverage per orbit. The objective function therefore is:

$$J = -e_0 \quad (11)$$

The states, $\mathbf{x}(t)$, and controls, $\mathbf{u}(t)$, as well as bounds on these variables are defined as:

$$[0.2 \text{ AU} \ 0 \ 0 \ 0]^T \leq \mathbf{x}(t) = [a \ e \ \omega \ t]^T \leq [\text{AU} \ 0.99 \ 2\pi \ 4\pi]^T \quad (12)$$

$$[0 \ -1]^T \leq \mathbf{u}(t) = [n_r \ n_t]^T \leq [1 \ 1]^T \quad (13)$$

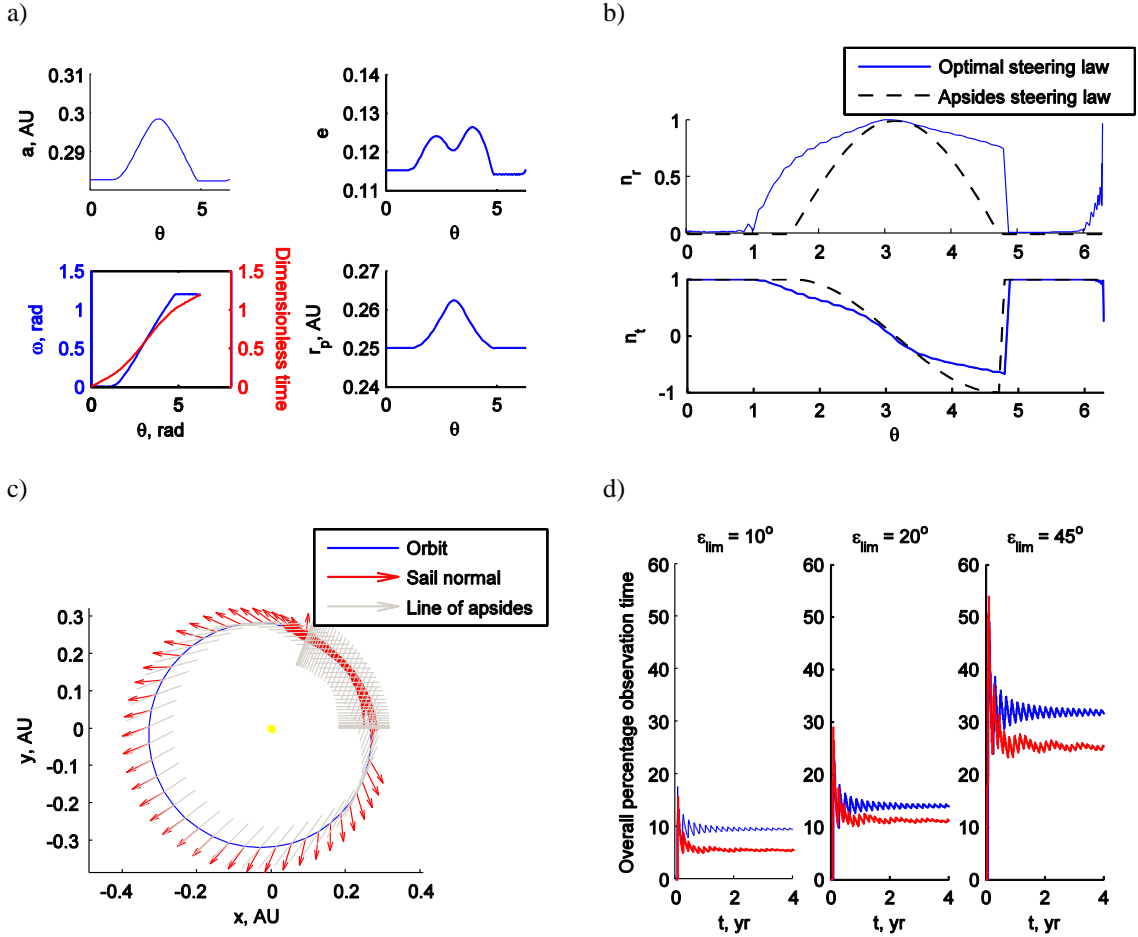


Figure 8 Optimal heliocentric Earth-following orbit for $\beta = \beta_{S,J,high}$. a) Evolution of Keplerian elements with r_p the perihelion radius. b) Optimal steering law. c) Orbit evolution. d) Surveillance zone analysis for heliocentric Earth-following orbit (upper blue line) and Keplerian reference orbit (lower red line).

The dynamics are defined in Eq. (1) and the event constraints are the required conditions defined for heliocentric Earth-following orbits in Eq. (2) as well as $\omega_0 = t_0 = 0$. Finally, two path constraints are included to ensure that the norm of the control vector is unity and that perihelion is always larger than 0.25 AU:

$$\begin{aligned} |\mathbf{u}(t)| &= 1 \\ a(1-e) &\geq 0.25 \text{ AU} \end{aligned} \quad (14)$$

The initial guess to initialise the optimal control problem is taken equal to the heliocentric Earth-following orbit found in the previous section, i.e. with time-varying semi-major axis and eccentricity and with an apsides steering law. To limit the number of results presented, Figure 8 only shows the outcome for $\beta = \beta_{st,high}$. Figure 8b and Figure 8c clearly show the difference between the apsides steering law and the optimal steering law: thrusting extends beyond the feasible domain for apsides steering, i.e. beyond $\frac{1}{2}\pi \leq \theta \leq \frac{3}{2}\pi$, and is more radially directed than the apsides steering law. When considering the time spent in the surveillance zone defined in the previous section and comparing it to an equally sized Keplerian orbit, it appears that the Earth-following orbit increases the time spent in the surveillance zone by a factor 1.29, compared to 1.18 for the apsides steering law.

The increase in surveillance zone coverage for heliocentric Earth-following orbits with respect to Keplerian orbits is promising. When requiring continuous coverage in the surveillance zone through the use of multiple spacecraft phased in the heliocentric orbit, the Earth-following orbits could, for example, allow a reduction in the required number of spacecraft to achieve this. Although the improvements achievable with a Sunjammer-type sail performance may be moderate, significant improvements can be expected from more advanced solar sails. However, as mentioned at the start of this section, care should be taken when using Lagrange equations as the perturbing sail acceleration becomes large with respect to the solar gravitational acceleration and the assumptions for the Lagrange equations break down.

SUN-EARTH LINE CONFINED SOLAR SAIL MANIFOLDS

The second type of novel application of solar sails for space weather monitoring and/or forecasting are Sun-Earth line confined solar sail manifolds: a solar sail acceleration is used to alter the course of the unstable subward manifolds associated to solar sail Halo orbits around a sub- L_1 point to travel upstream of coronal mass ejections and as such provide advanced warnings for space weather events.

Solar sail circular restricted three-body problem

The analyses start from the definition of the well-known circular restricted three-body problem (CR3BP), which describes the motion of an infinitely small mass, m , (here, the solar sail) under the influence of the gravitational attraction of two much larger masses, m_1 and m_2 (here, the Sun and Earth, respectively). [20] The reference frame employed is shown in Figure 9 and the corresponding motion of a solar sail is governed by the following equations of motion: [13]

$$\ddot{\mathbf{r}} + 2\boldsymbol{\omega} \times \dot{\mathbf{r}} + \boldsymbol{\omega} \times (\boldsymbol{\omega} \times \mathbf{r}) = \mathbf{a}_s - \nabla V \quad (15)$$

with V the gravitational potential and all other definitions provided in Figure 9. Furthermore, new units are introduced in the CR3BP: the sum of the two larger masses is taken as the unit of mass, i.e. $m_1 + m_2 = 1$. Then, with the mass ratio $\mu = m_2 / (m_1 + m_2)$, the masses of the large bodies become $m_1 = 1 - \mu$ and $m_2 = \mu$. For the Sun-Earth system, $\mu = 3.0404 \cdot 10^{-6}$ (i.e. also including the Moon's mass). As unit of length, the distance between the main bodies is selected, and $1/\omega$ is chosen as unit of time, yielding $\omega = 1$, and so one year is represented by 2π . Finally, an ideal solar sail model is once again assumed, defining the solar sail acceleration, \mathbf{a}_s , as:

$$\mathbf{a}_s = \beta \frac{1-\mu}{r_1^2} (\hat{\mathbf{r}}_1 \cdot \hat{\mathbf{n}})^2 \hat{\mathbf{n}} \quad (16)$$

Following Reference [13], the centripetal acceleration $\boldsymbol{\omega} \times (\boldsymbol{\omega} \times \mathbf{r})$ in Eq. (15) can be written as the gradient of a scalar potential function, $\Phi = -\frac{1}{2} \|\boldsymbol{\omega} \times \mathbf{r}\|^2$. Furthermore, given that the gravitational potential is:

$$V = -\left(\frac{1-\mu}{r_1} + \frac{\mu}{r_2}\right) \quad (17)$$

the gravitational and centripetal potential functions can be combined into a new, effective potential, U :

$$U = -\frac{x^2 + y^2}{2} - \left(\frac{1-\mu}{r_1} + \frac{\mu}{r_2}\right) \quad (18)$$

The new set of equations of motion then become:

$$\ddot{\mathbf{r}} + 2\boldsymbol{\omega} \times \dot{\mathbf{r}} = \mathbf{a}_s - \nabla U \quad (19)$$

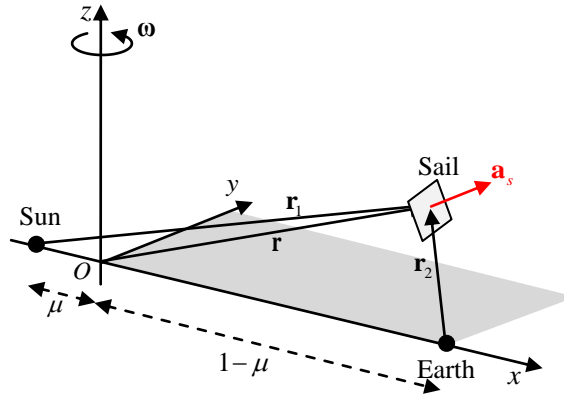


Figure 9 Schematic of circular restricted three-body problem.

Sub- L_1 point

The sub- L_1 point mentioned at the start of this section is a particular equilibrium point solution to Eq. (19). These equilibria can be found by setting $\ddot{\mathbf{r}} = \dot{\mathbf{r}} = 0$. For $\mathbf{a}_s = 0$, this yields the classical five Lagrange points, while for $\mathbf{a}_s \neq 0$ additional artificial equilibrium points (AEPs) can be found. The required solar sail acceleration to maintain an arbitrary AEP in the CR3BP is then given by:

$$\mathbf{a}_s = \nabla U \quad (20)$$

The required direction of this solar sail acceleration and the required solar sail lightness number can also be derived: [13]

$$\hat{\mathbf{n}} = \frac{\nabla U}{|\nabla U|} \quad (21)$$

$$\beta = \frac{r_1^2}{1-\mu} \frac{\nabla U \cdot \hat{\mathbf{n}}}{(\hat{\mathbf{r}}_1 \cdot \hat{\mathbf{n}})^2} \quad (22)$$

Since the point of interest in this work is the sub- L_1 point which is located along the Sun-Earth line, sunward of the classical L_1 point, its position coordinate will be $\mathbf{r} = [x_{\text{sub-}L_1} \ 0 \ 0]^T$. From Eq. (21) it then

follows that $\hat{\mathbf{n}} = [1 \ 0 \ 0]^T$, requiring the sail to be oriented perpendicular to the Sun-Earth line, and Eq. (22) reduces to:

$$\beta = \frac{(\mu + x_{\text{sub-L}_1})^2}{(1-\mu)} \left(-x_{\text{sub-L}_1} + \frac{\mu(x_{\text{sub-L}_1} - (1-\mu))}{\left((x_{\text{sub-L}_1} - (1-\mu))^2\right)^{\frac{3}{2}}} + \frac{(1-\mu)(\mu + x_{\text{sub-L}_1})}{\left((\mu + x_{\text{sub-L}_1})^2\right)^{\frac{3}{2}}} \right) \quad (23)$$

By substituting the lightness number of the Sunjammer solar sail, Eq. (23) can be solved numerically for the location of the sub-L₁ point, see Table 2. The table shows that, by positioning the Sunjammer solar sail at this sub-L₁ point, the warning time for space weather events can be increased by a factor 1.67-1.83 compared to existing satellites at the classical L₁ point.

Table 2 Sunjammer sub-L₁ data.

β	x - position sub-L ₁ point	Distance from Earth, km	Increase in warn- ing time over L ₁
0.0388	0.9833	2,496,371	1.67
0.0455	0.9816	2,747,104	1.83

Solar sail Halo orbits

Similar to Halo orbits around the classical co-linear Lagrange points, solar sail Halo orbits can be found around sub-L₁ points. [21, 22] Here, the approach described in Reference [21] is adopted, particularly the case where the attitude of the sail in the Halo orbit is assumed to be equal to its attitude at the sub-L₁ point, i.e. $\mathbf{n} = [1 \ 0 \ 0]^T$, so perpendicular to the Sun-Earth line. The first step is to approximate the equations of motion in Eq. (19) in the neighborhood of the sub-L₁ point by linearizing the equations of motion and expanding the combination of the effective potential and solar sail acceleration terms to third order with a Taylor series expansion. Subsequently, the Lindstedt-Poincare method is used to find the third order approximate periodic solution to this dynamical system by cancelling secular terms and matching the in-plane and out-of-plane frequencies.

Details on the method can be found in Reference [21]. For brevity, this paper only provides the results, see Figure 10, which shows five solar sail Halo orbits for different out-of-plane amplitudes, Z (in CR3BP units) and for both $\beta_{SJ,low}$ and $\beta_{SJ,high}$. In the work by K echichian and co-authors [17] the manifolds of a Halo orbit around the classical L₁ point with out-of-plane amplitude $Z = 0.0027$ is considered, hereafter referred to as the ballistic reference Halo orbit. The solar sail Halo orbit around the sub-L₁ point with the same out-of-plane amplitude is highlighted in blue in Figure 10 and will be considered for further investigations and comparison purposes.

Since the orbits in Figure 10 are only periodic approximations to the solutions of the full nonlinear system (i.e. Eq. (19)), the orbit quickly diverges when integrating its initial conditions in Eq. (19), see the red dashed line in Figure 11a. A differential correction scheme, see Reference [23], is therefore employed to adjust the initial conditions in such a way that true periodic solar sail Halo orbits are found. The result is shown by the light-blue, thick line in Figure 11, which shows only minor differences with the approximated solution (thin blue line). The figure also includes the ballistic reference Halo orbit considered in Reference [17] (black dashed line).

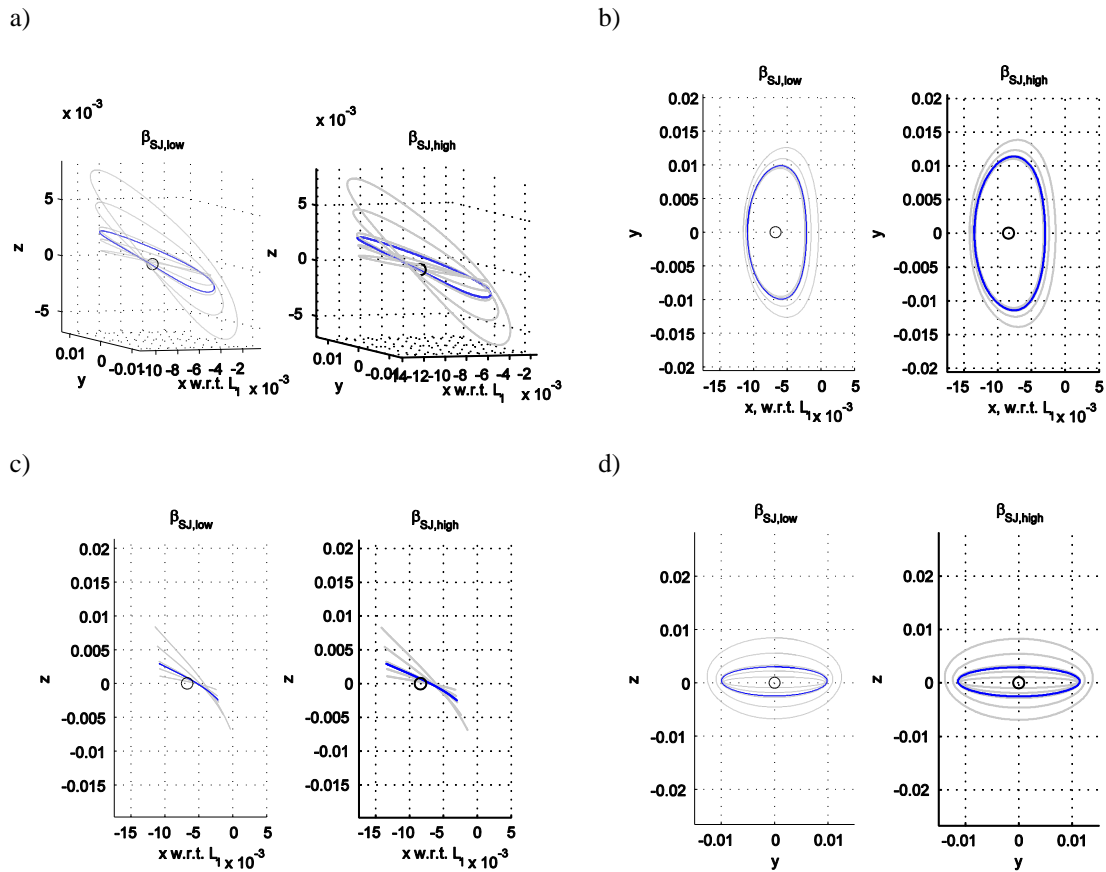


Figure 10 Approximated solar sail Halo orbits for $\beta_{SJ,low}$ and $\beta = \beta_{SJ,high}$ and out-of-plane amplitude $Z = 0.001, 0.002, 0.0027$ (in blue), $0.003, 0.005, 0.0075$. The sub- L_1 point is indicated by a round marker.

Unstable invariant manifolds

The last step in the design process of Sun-Earth line confined solar sail manifolds is the generation of the actual invariant manifolds associated with the solar sail Halo orbit in Figure 11. Since the theory of invariant manifolds and the approach to find these manifolds is described extensively in the literature (see for example Reference [24]), details are omitted here. It is just mentioned that, at first, the attitude of the sail in the manifolds is the same as in the Halo orbits, i.e. $\mathbf{n} = [1 \ 0 \ 0]^T$, and that we are particularly interested in the unstable manifolds that evolve in the direction of the Sun. As discussed in the introduction, under the correct circumstances, these manifolds stay close to the Sun-Earth line, while traveling ‘up-stream’ of the coronal mass ejection, potentially increasing the warning time for space weather events compared to spacecraft at the classical L_1 point as well as to a static solar sail at the sub- L_1 point or a solar sail in a Halo orbit around the sub- L_1 point. These unstable, sunward manifolds are shown in Figure 12a together with the manifolds that wind off the ballistic reference Halo orbit.

Surveillance zone analysis

In Reference [17], a manifold is considered useful for space weather forecasting as long as it resides within a cylinder of 4 Sun radii centered around the Sun-Earth line. This cylinder is hereafter referred to as

the surveillance zone. The manifolds in Figure 12a are truncated when the manifold leaves this surveillance zone, which is also evident from Figure 12b. Most important is how far upstream of the coronal mass ejections this occurs: the further upstream the manifold leaves the surveillance zone, the larger the warning time for a space weather event. Considering $\beta_{SJ,low}$, the manifold that extends farthest upstream reaches $x = -0.0290$ with respect to the classical L_1 point. This means that the warning time compared to spacecraft at L_1 can be increased by a factor 3.90, see also Figure 12c. For $\beta_{SJ,high}$ this factor is even slightly larger, 4.02. Note that the manifold number in Figure 12c and d is measured in the solar sail Halo orbit starting from the Sun-side crossing of the (x, z) -plane and continues in clockwise direction. Furthermore, the red manifold in Figure 12b-d highlights the manifold that enables the largest warning time, while the green manifold indicates the manifold that resides longest within the surveillance zone. It is clear that these do not overlap, i.e. the manifold with the largest warning time does not enable the longest stay time.

Comparing the results with the performance of the ballistic reference manifolds (in grey in Figure 12), it becomes clear that the increase in warning time enabled by a solar sail is not significant: the ballistic case increases the warning time by a factor 3.84. However, what the sail does enable is a longer stay time in the surveillance zone, as is evident from Figure 12b. Although much time is spent in close proximity of the solar sail Halo orbit, also the time further upstream of the coronal mass ejection is extended.

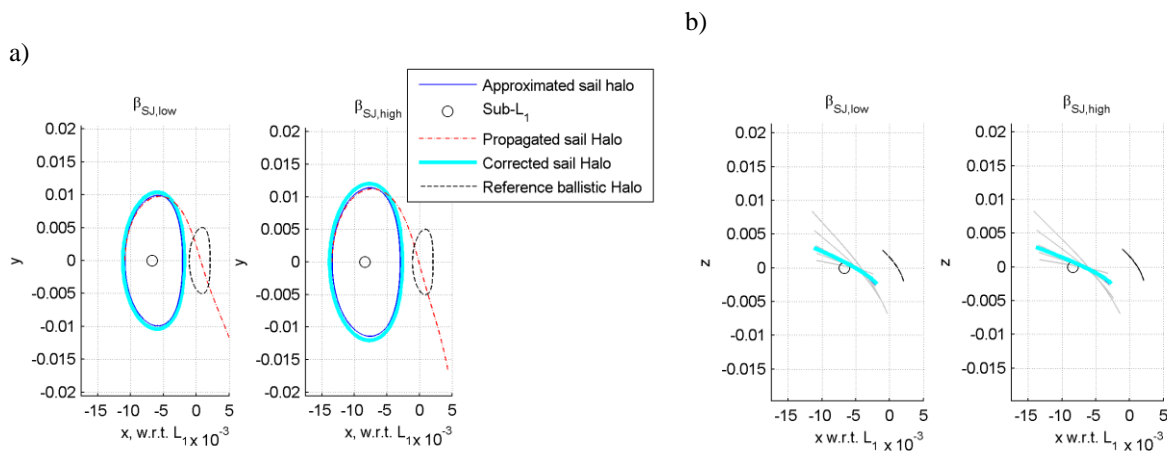


Figure 11 Differential correction scheme results and ballistic reference Halo orbit.

Pitched solar sail in manifolds

To investigate whether the performance of the solar sail can be increased further, this section pitches the solar sail *in the manifold* at a *constant* angle with respect to the Sun-Earth line. This angle is referred to as the cone angle and is defined in Figure 13. The sail is thus only pitched in the ecliptic plane, generating no acceleration component out-of-the ecliptic, and for $\alpha = 0$, the results as presented in the previous section can be obtained. When varying the value for α , the performance as shown in Figure 14 can be obtained. The figure indicates the maximum increase in warning time that any of the manifolds of the solar sail Halo orbit can establish. As a reference, Figure 14 also includes the performance of the ballistic reference manifolds (i.e. the previously mentioned factor of 3.84). It then immediately becomes clear that, when pitching the solar sail, significant improvements over the ballistic concept can be achieved: for a pitch angle of -33.2 deg and -32.9 deg for $\beta_{SJ,low}$ and $\beta_{SJ,high}$, respectively, the warning time compared to a spacecraft at L_1 can be increased by a factor 7.05 and 7.74. Specific details are provided in the first three rows of Table 3 and in Figure 15. The red manifold again highlights the manifold that enables the largest warning time, while the green manifold indicates the manifold that resides longest within the surveillance zone. This time, these two types of manifold almost coincide.

While the results in Figure 15 show a significant improvement in the warning time for space weather events, the assumption of a pitched sail comes at the cost of a much shorter stay time in the surveillance zone, see Figure 15d. However, as indicated in the introduction of the paper, it is envisaged that the concept of Sun-Earth line confined manifolds for space weather monitoring/forecasting is enabled by replenishing the best-performing manifold with SpaceChips from a solar sail platform in a Halo orbit around sub- L_1 . With the production cost and weight of these SpaceChips being very low, the disadvantage of a short stay time is expected to be outweighed by the large increase in warning time that this concept enables.

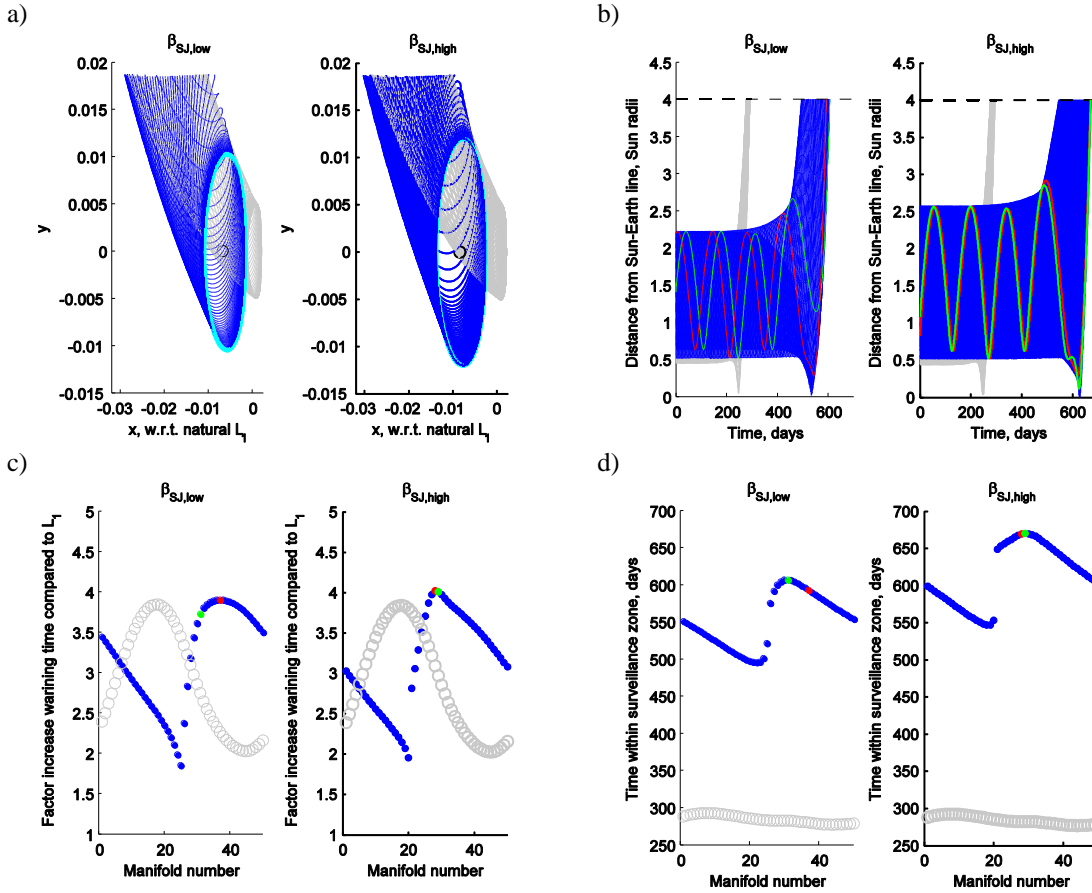


Figure 12 Solar sail manifolds with sail perpendicular to Sun-Earth line (blue) and ballistic reference manifolds (grey). The red manifold maximizes the warning time, the green manifold maximizes the time in the surveillance zone. a) (x,y) -projection. b) Distance from the Sun-Earth line. c) Increase in warning time compared to L_1 . d) Time within surveillance zone.

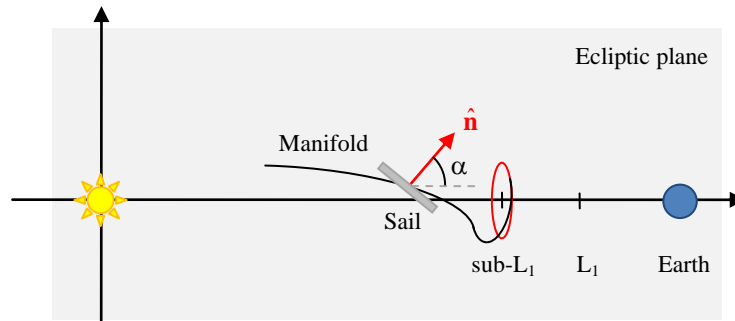


Figure 13 Definition of cone angle, α .

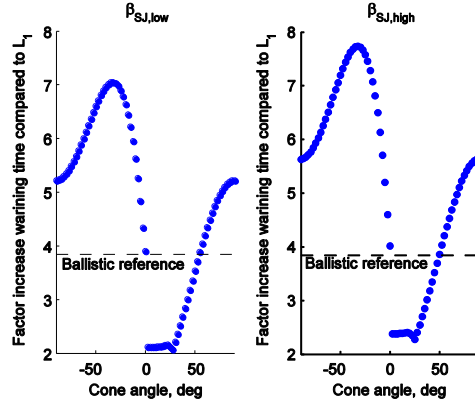


Figure 14 Increase in warning time compared to L_1 point with pitched sail.

Table 3 Solar sail manifold data for constant cone angle and optimal steering law.

	$\beta_{SJ,low}$	$\beta_{SJ,high}$
Constant cone angle		
Cone angle	-33.2 deg	-32.9 deg
Factor increase warning time compared to L_1	7.05	7.74
Time in manifold, days	102.2	101.1
Optimal steering law		
Factor increase warning time compared to L_1	8.16	9.19
Time in manifold, days	213.0	213.1

Optimal steering law in manifolds

The steering law of a constant cone angle as assumed in the previous section allows the use of low control authority devices such as SpaceChips. However, as mentioned in the introduction of the paper, another option could be to insert a conventional sailcraft like Sunjammer into the best-performing manifold towards the end-of-life to enable further improved observations at the end of the mission. In such a case, much higher control authority would be available. Therefore, this section investigates what the optimal control law would be to achieve the maximum increase in warning time, i.e. to travel as far upstream of the coronal mass ejection as possible. To that end, the accompanying optimal control problem is solved that minimizes:

$$J = x_f \quad (24)$$

where x_f is the final x -coordinate, i.e. upon leaving the 4 Sun radii surveillance zone. Since the optimal control problem is described in the CR3BP, the states and controls are defined as:

$$\begin{bmatrix} 1-\mu-0.1 \\ -0.1 \\ -0.1 \\ -0.2 \\ -0.2 \\ -0.2 \end{bmatrix} \leq \mathbf{x}(t) = \begin{bmatrix} x \\ y \\ z \\ \dot{x} \\ \dot{y} \\ \dot{z} \end{bmatrix} \leq \begin{bmatrix} 1-\mu \\ 0.1 \\ 0.1 \\ 0.2 \\ 0.2 \\ 0.2 \end{bmatrix}, \quad \begin{bmatrix} -1 \\ -1 \\ -1 \end{bmatrix} \leq \mathbf{u}(t) = \begin{bmatrix} n_x \\ n_y \\ n_z \end{bmatrix} \leq \begin{bmatrix} 1 \\ 1 \\ 1 \end{bmatrix} \quad (25)$$

and the dynamics are prescribed by Eq. (19).

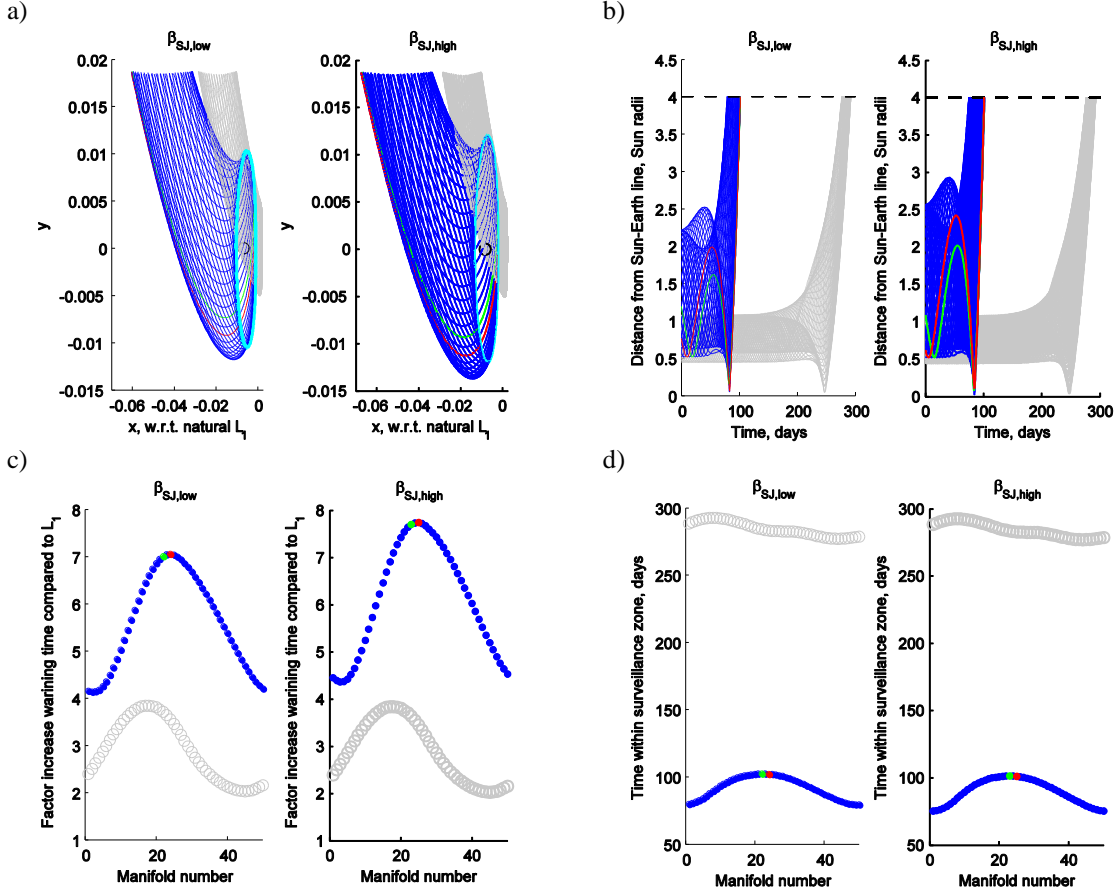


Figure 15 Solar sail manifolds with constant cone angle -33.2 deg ($\beta_{S,J,low}$) and -32.9 deg ($\beta_{S,J,high}$) (blue) and ballistic reference manifolds (grey). The red manifold maximizes the warning time, the green manifold maximizes the time in the surveillance zone. a) (x,y) -projection. b) Distance from the Sun-Earth line. c) Increase in warning time compared to L_1 . d) Time within surveillance zone.

Event constraints can be defined where the initial state-vector, \mathbf{x}_0 , should coincide with the location on the solar sail Halo orbit at time $t = t_0$. This location is found through an interpolation of a large state matrix that provides the position and velocity vectors along the Halo orbit for a range of time values. Note that $0 \leq t \leq t_p$ with t_p the period of the solar sail Halo orbit and $t = 0$ coinciding with the Sun-side crossing of the Halo orbit with the (x, z) -plane. An additional event constraint should be defined on the final state-vector, \mathbf{x}_f , such that the trajectory terminates at the edge of the surveillance zone:

$$\sqrt{y_f^2 + z_f^2} = 4R_s \quad (26)$$

with R_s the radius of the Sun. Finally, a set of path constraints ensures that the normal of the control vector equals unity, no acceleration component is generated in the direction of the Sun, the solar sail stays within the surveillance zone and the trajectory does not move too far downstream (i.e. not beyond classical L_1):

$$\begin{aligned}
\sqrt{n_x^2 + n_y^2 + n_z^2} &= 1 \\
\hat{\mathbf{r}}_1 \cdot \hat{\mathbf{n}} &\geq 0 \\
0 \leq \sqrt{y^2 + z^2} &\leq 4R_s \\
0 \leq x &\leq x_{L_1}
\end{aligned} \tag{27}$$

The solution to the optimal control problem is obtained with PSOPT by using the red manifolds in Figure 15 as initial guess. The results are provided in the last two rows of Table 3 and in Figure 16. The arrows in Figure 16a indicate the direction of the solar sail acceleration and show a very smooth optimal steering law. Furthermore, Figure 16b highlights the fact that the optimized trajectory allows a longer stay time within the surveillance zone than the constant cone angle steering law. Finally, and most importantly, Table 3 shows a further increase in the warning time for space weather events: for $\beta_{SJ,low}$ and $\beta_{SJ,high}$, the warning time can be increased by a factor 8.16 and 8.19 compared to observations from the L_1 point, resulting in a maximum warning time of approximately 4-8 and 4.5-9 hours, respectively.

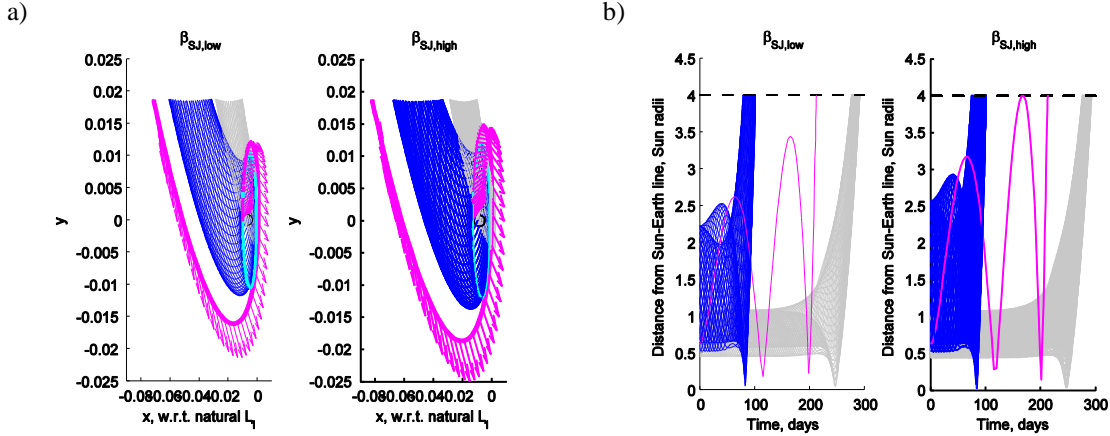


Figure 16 Solar sail manifolds with optimal control law (magenta), constant cone angle (blue) and ballistic reference (grey). a) (x,y) -projection. b) Distance from the Sun-Earth line.

CONCLUSIONS

In this paper, two novel solar sail concepts for space weather forecasting have been presented: heliocentric Earth-following orbits and Sun-Earth line confined solar sail manifolds. The first concept has shown the possibility to rotate the line of apsides of a heliocentric orbit with a solar sail such that aphelion always coincides with the Sun-Earth line. As such, the observation time of the region between Sun and Earth is increased, allowing for improved observations of space weather events compared to an inertially fixed Keplerian orbit. A simple apsides steering law can already increase the time spent within a predefined cone around the Sun-Earth line by a factor 1.18 for a sail performance equal to that of the Sunjammer solar sail. For an optimal solar sail steering law, this increases further to a factor 1.29. The result is that, when requiring continuous observation around the Sun-Earth line through the use of a phased constellation of satellites, the heliocentric Earth-following orbits may require one or two spacecraft less than a Keplerian orbit.

The second concept has exploited a solar sail acceleration to alter the course of the unstable, sunward manifolds of a Halo orbit around a sub- L_1 point. Again, for a Sunjammer like performance, the sub- L_1 point is located a factor 1.67-1.83 farther from the Earth than the classical L_1 point, already allowing a substantial increase in the warning time for space weather events. By keeping the solar sail acceleration vector along the Sun-Earth line, Halo orbits around the sub- L_1 point have been found and the unstable sunward manifolds of these Halo orbits travel upstream of the coronal mass ejections. This increases the warning time by a factor 3.90-4.02. However, the ballistic manifolds winding off an equally sized ballistic Halo orbit around the classical L_1 point can achieve a similar increase in the warning time. Therefore, the solar sail has been pitched at a constant angle with respect to the Sun-Earth line, significantly increasing the warning time: up

to 7.74 times the warning time from the L_1 point. However, this comes at the cost of a much shorter stay time in the surveillance zone, requiring a more frequent replenishment of probes into the manifold to ensure a continuous advanced warning time. A final improvement has been achieved by finding the optimal steering law for the solar sail to travel as far as possible upstream of the space weather events. This resulted in a maximum increase in the warning time by a factor 8.19 compared to satellites at L_1 , leading to a total warning time of 4.5-9 hours as well as a longer stay time in the surveillance zone compared to the constant cone angle steering law.

ACKNOWLEDGMENTS

This work was funded by the European Research Council Advanced Investigator Grant-227571: Visionary Space Systems: Orbital Dynamics at Extremes of Spacecraft Length-Scale.

REFERENCES

- ¹ M. Hapgood, Nano Satellite Beacons for Space Weather Monitoring: Final Report (SWNS-RAL-RP-0001), 2008.
- ² D. Selva, D. Krejci, A Survey and Assessment of the Capabilities of Cubesats for Earth Observation, *Acta Astronautica*, 74 (2012) 50-68.
- ³ C. Fong, Y. Liou, S. Chi, Space-Based Global Weather Monitoring System: FORMOSAT-3/COSMIC Constellation and Its Follow-On Mission, *Journal of Spacecraft and Rockets*, 46 (2009) 883-891.
- ⁴ B.E. Goldstein, A. Buffington, A.C. Cummings, R. Fisher, B.V. Jackson, P.C. Liewer, R.A. Mewaldt, M. Neugebauer, A Solar Polar Sail Mission: Report of a Study to Put a Scientific Spacecraft in a Circular Polar Orbit About the Sun, *SPIE International Symposium on Optical Science, Engineering and Instrumentation*, (1998).
- ⁵ M. Macdonald, G.W. Hughes, C.R. McInnes, A. Lyngvi, P. Falkner, A. Atzei, A Solar Sail Technology Reference Study, *Journal of Spacecraft and Rockets*, 43 (2006) 960-972.
- ⁶ D.M. Rust, Heliospheric Links Explorer (HELIX), *Acta Astronautica*, 39 (1996) 217-227.
- ⁷ J.L. West, The GeoStorm Warning Mission: Enhanced Opportunities Based on New Technology, 14th AAS/AIAA Spaceflight Mechanics Conference, AAS-04-102, Maui, Hawaii, 2004.
- ⁸ R. McKay, M. Macdonald, F. Bosquillon de Frescheville, M. Vasile, C. McInnes, J. Biggs, Non-Keplerian Orbits Using Low Thrust, High ISP Propulsion Systems, 60th International Astronautical Congress, IAC-09.C1.2.8, Daejeon, South Korea, 2009.
- ⁹ R.J. McKay, M. Macdonald, J. Biggs, C. McInnes, Survey of Highly Non-Keplerian Orbits with Low-Thrust Propulsion, *Journal of Guidance, Control, and Dynamics*, 34 (2011).
- ¹⁰ C.G. Sauer, The L1 Diamond Affair, 14th AAS/AIAA Space Flight Mechanics Conference, Maui, Hawaii, 2004.
- ¹¹ Y. Tsuda, O. Mori, R. Funase, H. Sawada, T. Yamamoto, T. Saiki, T. Endo, J. Kawaguchi, Flight Status of IKAROS Deep Space Solar Sail Demonstrator, *Acta Astronautica*, 69 (2011) 833-840.
- ¹² L. Johnson, M. Whorton, A. Heaton, R. Pinson, G. Laue, C. Adams, NanoSail-D: A Solar Sail Demonstration Mission, *Acta Astronautica*, 68 (2011) 571-575.
- ¹³ C.R. McInnes, *Solar Sailing: Technology, Dynamics and Mission Applications*, Springer-Praxis Books in Astronautical Engineering, Springer-Verlag, Berlin, 1999.
- ¹⁴ C. Bidy, T. Svitek, LightSail-1 Solar Sail Design and Qualification, *Proceedings of the 41st Aerospace Mechanisms Symposium*, Pasadena, CA, 2012.
- ¹⁵ D.J. Barnhart, T. Vladimirova, M.N. Sweeting, Very-Small-Satellite Design for Distributed Space Missions, *Journal of Spacecraft and Rockets*, 44 (2007) 1294-1306.
- ¹⁶ C. Colombo, C. Lucking, C. McInnes, Orbital dynamics of high area-to-mass ratio spacecraft with J2 and solar radiation pressure for novel Earth observation and communication services, *Acta Astronautica*, 81 (2012) 137-150.
- ¹⁷ J.A. Kechichian, E.T. Campbell, M.F. Werner, E.Y. Robinson, Solar Surveillance Zone Population Strategies with Picosatellites Using Halo and Distant Retrograde Orbits, *Acta Astronautica*, 56 (2005) 495-506.
- ¹⁸ P. Fortescue, J. Stark, *Spacecraft Systems Engineering*, Wiley, New York, 1995.
- ¹⁹ V.M. Becerra, Solving Complex Optimal Control Problems at No Cost with PSOPT, *IEEE Multi-conference on Systems and Control*, Yokohama, Japan, 2010.
- ²⁰ R.H. Battin, *An Introduction to the Mathematics and Methods of Astrodynamics*, Revised Edition, American Institute of Aeronautics and Astronautics, Inc., Reston, USA, 1999.
- ²¹ H. Baoyin, C. McInnes, Solar Sail Halo Orbits at the Sun-Earth Artificial L_1 -point, *Celestial Mechanics and Dynamical Astronomy*, 94 (2006) 155-171.
- ²² T.J. Waters, C.R. McInnes, Periodic Orbits Above the Ecliptic in the Solar-Sail Restricted Three-Body Problem, *Journal of Guidance, Control, and Dynamics*, 30 (2007) 687-693.
- ²³ K.C. Howell, Three-dimensional, periodic, 'Halo' orbits, *Celestial Mechanics*, 32 (1983) 53-71.
- ²⁴ W.S. Koon, M.W. Lo, J.E. Marsden, S.D. Ross, *Dynamical Systems, the Three-Body Problem and Space Mission Design*, 2006.